American Mineralogist, Volume 102, pages 1881–1893, 2017

Insights into solar nebula formation of pyrrhotite from nanoscale disequilibrium phases produced by H_2S sulfidation of Fe metal

Zack Gainsforth[1,*], Dante S. Lauretta[2], Nobumichi Tamura[3], Andrew J. Westphal[1], Christine E. Jilly-Rehak[1], and Anna L. Butterworth[1]

[1]Space Sciences Laboratory, University of California at Berkeley, Berkeley, California 94720, U.S.A.
[2]Lunar and Planetary Laboratory, University of Arizona, Tucson, Arizona 85721, U.S.A.
[3]Advanced Light Source, Lawrence Berkeley National Laboratory, Berkeley, California 94720, U.S.A.

Abstract

Lauretta (2005) produced sulfide in the laboratory by exposing canonical nebular metal analogs to H_2S gas under temperatures and pressures relevant to the formation of the Solar System. The resulting reactions produced a suite of sulfides and nanophase materials not visible at the microprobe scale, but which we have now analyzed by TEM for comparison with interplanetary dust samples and comet Wild 2 samples returned by the Stardust mission. We find the unexpected result that disequilibrium formation favors pyrrhotite over troilite and also produces minority schreibersite, daubréelite, barringerite, taenite, oldhamite, and perryite at the metal-sulfide interface. TEM identification of nanophases and analysis of pyrrhotite superlattice reflections illuminate the formation pathway of disequilibrium sulfide. We discuss the conditions under which such disequilibrium can occur, and implications for formation of sulfide found in extraterrestrial materials.

Keywords: Pyrrhotite, troilite, sulfide, planetary science, TEM, XRD, H_2S, comet

Introduction

In the canonical model of the early inner Solar System, the first solids to form from the cooling nebula were produced by gas-solid condensation reactions. Initially, refractory phases such as alumina formed at temperatures above 1400 K. Continued condensation influenced the composition of the gas as atomic species were differentiated out of the gas phase into various solids (Lord 1965; Lewis 1972; Davis and Richter 2005). It is thought that at ~1000 K, most excess Fe had condensed into metal with a few wt% of Ni, Cr, P, and C, while most of the sulfur was bound in H_2S. As temperatures dropped below 713 K, the H_2S began to react with the nebular Fe to produce stoichiometric FeS, or troilite (Lauretta et al. 1996). Because the cosmochemical abundance of Fe is twice that of S (Lodders 2010), and because equilibrium calculations show that pyrrhotite cannot coexist with troilite and Fe metal in the presence of H_2S gas, it would not be possible to form pyrrhotite directly in equilibrium. Therefore, it was thought that pyrrhotite formed in the nebula only when troilite entered a region with excess H_2S and no metal and reacted at high temperature (Zolensky and Thomas 1995).

In this paper we consider an alternate pathway that likely operated in parallel and may be crucial for understanding the history of nanophase sulfide such as found in comets. Specifically, both troilite and pyrrhotite form simultaneously by the reaction of H_2S gas with metal under disequilibrium conditions for reasons that will become clear in the discussion. This idea is not without precedent. In general, disequilibrium is known to have a significant effect on mineral formation sequences and temperatures, so accounting for it can dramatically increase the accuracy of models (Carlson et al. 2015). It is known that pyrrhotite can form directly from iron metal when the sulfur fugacity (f_{S_2}) is very high (Imae 1994; Lauretta et al. 1996), though it is not clear that nebular conditions can supply a sufficiently high f_{S_2}. Pyrrhotite has also been formed directly from the gas phase when equilibrium is not reached (Osaka et al. 1976; Lauretta et al. 1996), though these experiements were not perfect analogs for the nebular environment.

We re-examine iron metal foils that have been sulfidized by H_2S gas as an analog for the sulfidation of nebular metal (Lauretta et al. 1996; Lauretta 2005). These foils have been previously studied at the micrometer scale, but until recently there has been little motivation to examine the nanoscale properties of this experiment. Recent work on interplanetary dust particles (IDPs, Dai and Bradley 2001; Westphal et al. 2009; Ogliore et al. 2010) and samples returned by the Stardust mission (Gainsforth et al. 2013, 2014, 2015; Stodolna et al. 2014; Ogliore et al. 2012) have made it apparent that we need a better understanding of superlattice structures, nanoscale element distribution, and crystal morphologies at the nanoscale to interpret comet samples.

Mineralogy of pyrrhotite

Troilite is stoichiometric FeS. At > 315 °C, it exists in the NiAs structure (hexagonal, space group $P6_3/mmc$): the sulfur atoms form a hexagonally close packed structure and the Fe occupies octahedral interstitial positions. At these temperatures, the spin of the Fe atoms is random (Wang and Salveson 2005). Below 315 °C, troilite undergoes an antiferromagnetic ordering transition whereby Fe and S atoms move on the order of half an angstrom from their original positions. This reduces the symmetry of the unit cell to hexagonal, $P\bar{6}2c$. The new unit cell is commonly referred to as troilite $2C$, since the c axis is twice the

* E-mail: zackg@ssl.berkeley.edu

0003-004X/17/0009–1881$05.00/DOI: http://dx.doi.org/10.2138/am-2017-5848

NiAs unit-cell length. Troilite 2*C* is the stable room-temperature form of stoichiometric FeS. When forming in sulfur-rich environments, superlattice structures (pyrrhotite) can form with Fe vacancies. For a full review of the pyrrhotite polytypes, we recommend Wang and Salveson (2005). For a detailed study of the phase diagram of pyrrhotite, we suggest Nakazawa and Morimoto (1971).

Pyrrhotite has the formula $Fe_{(1-\delta)}S$ where δ is called the iron deficit or vacancy parameter. Pyrrhotite structures have, at most, 1 of 8 Fe atoms absent, resulting in the structure Fe_7S_8 ($\delta = 0.125$) with the space group $F2/d$ and a unit cell four times longer than the NiAs unit cell (Putnis 1975). Thus, Fe_7S_8 is called pyrrhotite 4*C*. Intermediate vacancy densities form longer unit cells leading to 5*C*, 6*C*, and even 11*C* superlattices. In addition, there are several "*nC* " superlattices that show non-integer periodicities not easily described with the superlattice concept. Harries et al. (2011) found that Translation Interface Modulation (TIM) (Van Dyck et al. 1987) theory is a better framework for understanding pyrrhotite than restricting it to a set of superlattice structures. In the pyrrhotite TIM model, 4*C* unit cells are stacked as usual, but extra FeS layers without vacancies are inserted with non-integral periodicities leading to *nC* pyrrhotite. Figure 10 in Harries et al. (2011) gives a good visualization of how TIM works.

Sometimes, the pyrrhotite has significant disorder that streaks the diffraction patterns. (Nakazawa and Morimoto 1971; Harries et al. 2011; Pósfai et al. 2000). Nakazawa and Morimoto (1971) also found that pyrrhotite with a composition very close to troilite 2*C* (e.g., $Fe_{0.99}S$) can have very diffuse superlattice reflections where *n* cannot be exactly determined.

Troilite and pyrrhotite compositions are typically close to $Fe_{1-\delta}S$ but natural crystals often have substantial substitution of Cr, Ni, Co, Cu, and Zn for Fe, and Se can substitute for S. The partitioning of cations between iron sulfide and metal depends on the thermodynamic conditions during the sulfidation (Lauretta 2005). Specifically, when FeS forms from the sulfidation of Fe metal, we find that siderophile elements such as Co and Ni become more concentrated in the metal. Similarly, chalcophile elements such as Cu prefer the sulfide (MacLean and Shimazaki 1976; Li and Audétat 2012). Pentlandite, $(Fe,Ni)_9S_8$, space group $Fm\bar{3}m$, can also exsolve from sulfide with more than a few wt% Ni (Etschmann et al. 2004; Schrader et al. 2015).

Methods

Lauretta (2005) exposed metal foils to H_2S gas for 4.5 h at temperatures ranging from 400 to 1000 °C, which is above the 1*C* ↔ 2*C* transition temperature of 315 °C. The foils were then cooled to room temperature within 20 min using ultrahigh-purity He. The foils had a composition of 93.4 wt% Fe, 4.75 wt% Ni, 0.99 wt% Co, 0.89 wt% Cr, and 0.66 wt% P. The presence of minor Si phases in the reaction products suggests that some Si was also present in the metal. This composition falls within the range of compositions of meteoritic metals that experienced sulfidation, see, e.g., Tables 2 and 3 and Figure 11 in Lauretta and Buseck (2003). We extracted FIB sections from three of these foils (900, 500, and 400 °C) using an FEI Strata 235 Dual Beam focused ion beam (FIB) at the National Center for Electron Microscopy (NCEM) at the Lawrence Berkeley National Laboratory. The lamellae were initially 100–500 nm thick. We did EDS mapping at 80 and 200 keV using an FEI Titan with a 4-element Bruker silicon drift detector (SDD) with a solid angle of 0.6 sr and count rates between 5 and 100 kcps. We applied the Cliff-Lorimer method for element quantification and a thin film EDS absorption correction (Gainsforth 2016). Statistical uncertainties for major elements in metal and sulfide were generally 0.1%, smaller than uncertainties from absorption corrections.

The FIB lamella cut from the foil reacted at 900 °C was mounted on a beryllium grid allowing for quantification of Cu. The FIB lamellae cut from the 400 and 500 °C foils were mounted on Cu grids. Detection limits were typically <1000 ppm, depending on the element and host phase. On the 900 °C foil, since no superlattice reflections were found from the troilite, we assumed perfect stoichiometry: (Fe+Ni+Cr+Cu+Co)/S ≡ 1.000, and assumed the thickness to satisfy this condition. The original FIB section was cut to 500 nm, and the derived thickness was 506 nm. This same thickness was then applied to the other spectra on the lamella. We cut a foil from the sulfide formed at 500 °C that was 200 nm thick at the base. We assumed a 100 nm thickness in the center of the lamella, assuming that to be half the thickness of the lamella at the thickest point, and normalized thickness according to the number of Fe counts in the sulfide phases. We expect the relative thickness errors using this approach to be <10% but it is possible there could be a systematic error up to 30%. With this approach, we find the formula $Fe_{1-\delta}$ S to be satisfied with δ values between 0.04–0.12 as would be expected given the superlattice reflections seen in diffraction, though systematic errors could shift all δ values. After initial EDS work, the samples were further thinned in the FIB to allow for improved TEM imaging and selected-area electron diffraction (SAED). We did imaging and diffraction at 80 and 200 keV with the Titan and at 200 keV with a Zeiss Libra 200 MC with an in column Omega energy filter. SAED patterns from the Libra were energy filtered to sharpen the diffraction peaks.

We characterized larger regions of the foils using X-ray microdiffraction (μXRD) at beamline 12.3.2 at the Advanced Light Source synchrotron (Tamura et al. 2009). We used white beam (Laue) μXRD mapping for determining crystal orientations of coarse-grained material and monochromatic (mono) μXRD mapping for analyzing the fine-grained polycrystalline pyrrhotite. Laue maps were generated using an unfiltered beam directly from a superconducting bend magnet. Kirkpatrick-Baez mirrors were used to focus the beam and slits were used to collimate the beam at 0.5 × 0.5 μm and limit flux. Mono maps were acquired by inserting a four-bounce Si-111 monochromator and removing slits to provide a beam several micrometers across. The mono beam was then scanned while 2D μXRD patterns were acquired using a Dectris Pilatus 1M camera to simulate a broad X-ray source (on the order of 1 mm). Silicon and quartz were used to calibrate the diffraction geometry for Laue maps. Alumina was used to calibrate the diffraction geometry for mono maps. Data analysis was done using Python (Hunter 2007; Oliphant 2007; Pérez and Granger 2007; Van Der Walt et al. 2011) and XMAS (Tamura 2014).

Results

900 °C foil

Figure 1a shows an SEM/EDS map of the foil sulfidized at 900 °C after embedding and polishing. Fe sulfide encompasses unreacted Fe foil showing that the reaction was incomplete leaving some Fe metal at the core. Several phosphides are present within the sulfide in a ~30 μm thick layer near the metal/sulfide interface.

We chose a region at the metal/sulfide interface for μXRD that samples the metal, the fine-grained layer and neighboring coarse sulfides. Figure 1b shows how the fine-grained layer is sandwiched between the metal and coarse sulfide. A μXRD crystal orientation map (Fig. 1c) shows that the sulfide is preferentially oriented with the troilite *c* axis near the plane of the metal-sulfide interface, without any azimuthal constraint. The mean *c* axis orientation is 4° from the plane with a standard deviation of 20°.

The FIB section (Figs. 2a and 2b) only samples the metal and fine-grained layer and contains chromite, metal, and several sulfide crystals. All crystal domains are >1 μm across. The chromite crystal is euhedral, has end-member chromite composition (Supplemental[1] Table 1, TEM 01), and abuts sulfide and metal. The sulfide in contact with the chromite is Cr rich pyrrhotite with ~20 wt% Cr (Supplemental[1] Table 1, TEM 00), but the sulfide that is only

[1]Deposit item AM-17-95848, Supplemental Material. Deposit items are free to all readers and found on the MSA web site, via the specific issue's Table of Contents (go to http://www.minsocam.org/msa/ammin/toc/2017/Sep2017_data/Sep2017_data.html).

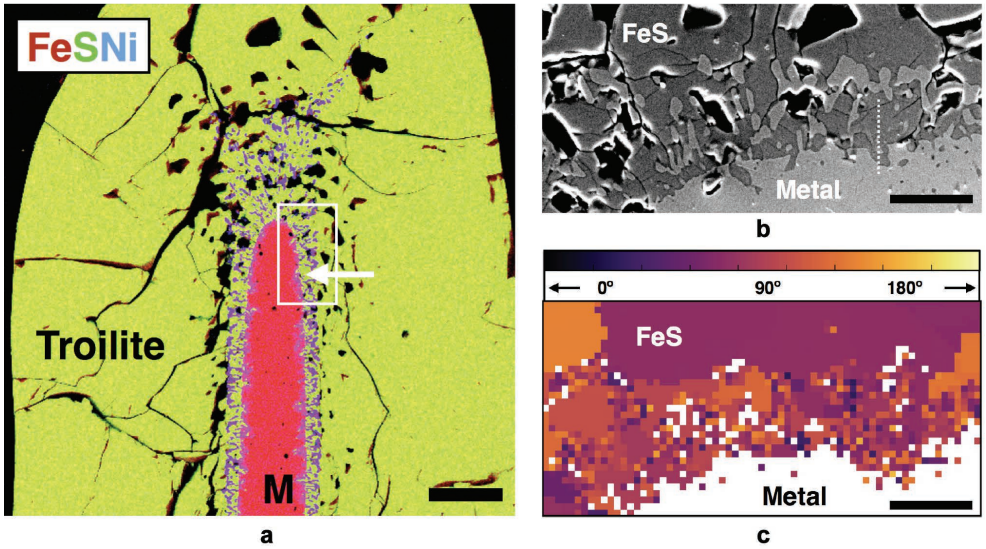

►**Figure 1.** (**a**) SEM/EDS map taken at 20 keV of the 900 °C foil with Fe (red), S (green), Ni (blue). Metal (M) is red. Troilite is green. Schreibersite is purple. The boxed area corresponds to **b** and the arrow indicates where the FIB lamella was cut. The scale bar is 100 μm. (**b**) Secondary electron image at 20 keV of a region selected for μXRD showing metal on the bottom, and sulfide on the top. The dotted line shows the location where the FIB section was removed. The scale bar is 25 μm. (**c**) Laue μXRD map of the foil sulfidized at 900 °C. The colors correspond to the angle between the troilite 001 axis and the approximate normal vector for the metal surface, such that 90° means the 001 axis is in the plane of the metal surface. White pixels did not give a satisfactory fit to troilite, often because the phase was metal. The scale bar is 25 μm.

in contact with the metal is troilite with 1–4 wt% Cr, Ni, Co and 0.2 wt% Cu. The troilites have perfect stoichiometry within error bars (cation/S = 1.00 and 1.01, see spectra TEM 02, 03 in Supplemental[1] Table 1, respectively) and no superlattice reflections in SAED patterns.

The metal has 30 wt% Ni near a grain boundary (spot 4), and closest to the sulfide (spot 5). The metal furthest from the sulfide, or alternately, closest to the chromite is less Ni rich (spot 6) with 20 wt% Ni. A SAED pattern (spot X) of the metal close to the chromite grain is shown in Figure 2c. The reflections marked as K have a *d*-spacing of 2.03 Å, consistent with kamacite (low-Ni BCC iron, 111 reflection). The reflections marked as T are measured to be 2.15 Å close to taenite (high-Ni FCC iron, 111 reflection). The

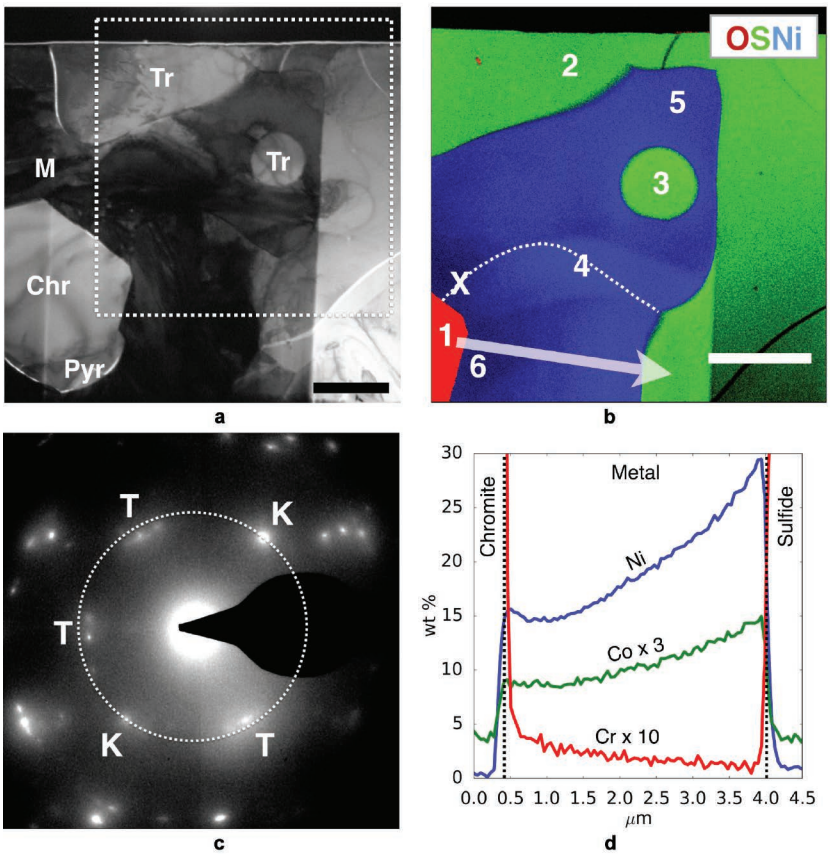

►**Figure 2.** (**a**) LAADF image of the 900 °C foil. Metal (M), troilite (Tr), pyrrhotite (Pyr), and chromite (Chr) are labeled. The dashed box corresponds to the region shown in **b**. The composition of Pyr is given in Supplemental[1] Table 1, TEM 00. The scale bar is 2 μm. (**b**) EDS view of 900 °C foil: O (red), S (green), Ni (blue) showing chromite (red), troilite (green), and FeNi metal (blue). 1–6 correspond to spectra TEM 01–06 in Supplemental[1] Table 1. The dotted line indicates a grain boundary in the metal. X is the location of the SAED pattern in **c**. The arrow indicates the line scan in **d**. The vertical line near to and perpendicular to the scale bar is a FIB curtaining effect from the metal. 2 μm scale bar. (**c**) SAED view of the metal showing kamacite reflections (K) at 2.03 Å and taenite reflections (T) at 2.14 Å; 2.03 Å circle. (**d**) Line scan (see arrow in **b**) 1.22 μm wide by 4.5 μm long showing Ni and Co concentration increase approaching the sulfide, but Cr decreases.

observation of the taenite FCC structure by SAED is consistent with the high Ni concentration observed by EDS. The BCC Fe could be from exsolution as the metal was quenched. The composition likely represents pure FCC Fe at 900 °C. The line scan plotted in Figure 2d shows that Ni, Co, and Cu (not plotted) are siderophile: the highest concentrations are in the metal. The Cr exhibits chalcophile behavior with higher concentration in the sulfide. The heterogeneity of the metal indicates that the system has not reached equilibrium.

500 °C foil

Figure 3a shows a region of the foil sulfidized at 500 °C and analyzed by μXRD. Unlike the foil sulfurized at 900 °C, the coarse-grained sulfide separated from the metal leaving a thin layer of fine-grained sulfide and phosphide crystals attached to the metal. During sample preparation epoxy impregnated the void spaces and shows as black in the SEM image. The fine-grained crystals are now so small that the orientation map (Fig. 3b) is insensitive to them, but many of the domains seen in μXRD can be matched against the coarse-grained crystals visible in SEM. The orientation map shows that the coarse crystals are oriented differently than in the foil sulfidized at 900 °C. The angles now average 34° out of the metal/surface plane, with most crystals oriented with their *c* axis pointing away from the metal, and some pointing toward the metal. The standard deviation of the orientations is 13° ignoring the polarity of the *c* axis direction (i.e., 135° is equivalent to 45°).

A μXRD monochromatic pattern obtained at 10 keV is more sensitive to the fine-grained component. The composition of pyrrhotite is usually determined by measuring the absolute *d*-spacing of the troilite 114 reflection (102 for the NiAs unit cell, Yund and Hall 1969). In addition to 114, we also used the troilite 112 reflection to avoid interferences with other phases. We found a range of compositions from troilite ($\delta = 0.00$) to $\delta = 0.11$ encompassing the pyrrhotite 5*C* and 6*C* field (de Villiers et al. 2009; de Villiers and Liles 2010).

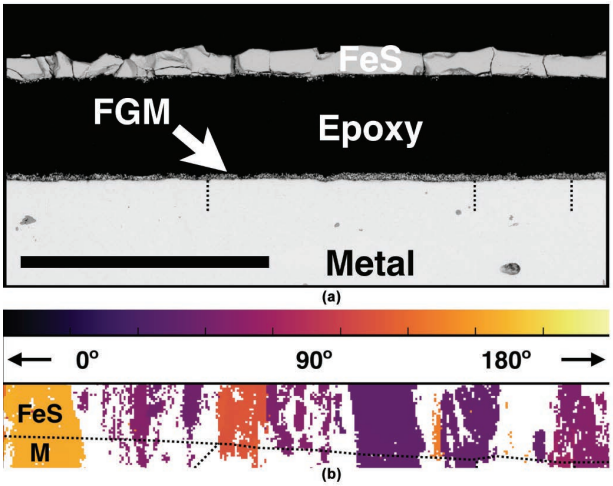

Figure 3. (**a**) Backscatter electron image at 10 keV of the foil sulfidized at 500 °C, showing the region studied with μXRD. FGM is fine-grained material comprising sulfides and phosphides. The scale bar is 100 μm. (**b**) Laue μXRD map of the same area, similar to Figure 1c. The XRD data was acquired with the sample tilted at 45° so the sulfide appears to overlap the metal. The dotted line shows the metal surface, and grain boundaries within the metal. The color legend shows the angle between the troilite 001 axis and the approximate metal surface normal vector, taken as the horizontal (XZ) plane in the image. 90° indicates the 001 vector is in the plane of the metal, and 0 or 180° indicates the troilite 001 vector is pointing away from the metal or toward it.

Figure 4a shows an SEM/EDS map of the region near where two FIB lamellae were cut. They included the metal, the fine-grained crystals, and the coarse sulfide layer. Figure 4b shows an EDS map of one of the FIB lamellae with numbered spots corresponding to the spectra in Supplemental[1] Table 2. The sulfide forms as tendrils extending away from from the metal and has a composition close to troilite but with 4 wt% Cr and 2 wt% Ni (spots 8 and 9). The sulfide frequently shows diffuse pyrrhotite 4*C* superlattice structure as can be seen in the SAED image in Figure 4c. Not shown in the figures are two tabular pyrrhotite grains from the coarse layer (Supplemental[1] Table 2, TEM 15 and 16).

Schreibersite, $(Fe,Ni)_3P$ (spots 7 and 14), is present both as spherical blebs and filamentous nanocrystals among the sulfide. In some cases it appears as nanorods with an aspect ratio >10. Phosphide within sulfide tends to have more rounded edges than phosphide between sulfides.

A $(Cr,Ni,Fe)_3S_4$ sulfide (spot 10) is surrounded by phosphide nanocrystals, and proximal to pyrrhotite. SAED is consistent with zone 110 of daubréelite ($FeCr_2S_4$).

Unlike the 900 °C foil, the metal does not show a strong enrichment in Ni near the metal/sulfide interface (spot 11) and diffraction indicates kamacite not taenite. All of the minor elements, Ni, P, and Cr are within 20% of the original metal composition just a few nanometers away from the interface, consistent with kamacite.

Figure 4d shows the complex interaction between the metal/sulfide/phosphide interface. The phosphides are interwoven with the sulfides as they extend out from the metal. The sulfide hosts a cobalt-rich phosphide compositionally consistent with barringerite, $(Fe,Ni,Co)_2P$ (Supplemental[1] Table 2, TEM 12), and a Si-rich phosphide compositionally close to perryite, $(Fe,Ni,Co)_8(P,Si)_3$, though not a perfect match (Supplemental[1] Table 2, TEM 13) because P > Si, whereas meteoritic perryite has Si > P (Lehner et al. 2010). However, Si and P occupy the same site in the perryite structure and it is plausible that it could have any ratio of P/Si (Okada et al. 1991).

Figure 4e shows examples of common features at the interface. A schreibersite bleb is forming off a metal promontory. A sulfide layer several nanometers thick is present on the surface of the metal everywhere, but not on the phosphide. A thin oxide layer is present outside the sulfide and phosphide consistent with a few angstroms thick layer that we would expect to see from momentary exposure to air (Pratt et al. 1994).

A faint Ni-rich whisker is visible on the left side of Figure 4e and is magnified in Figure 4f. The whisker is 10 × 80 nm in size and appears to be growing out of the metal surface. The slope of the metal changes on either side of the whisker showing that it is oriented relative to the metal and its topography. It has an oxide rim that may be due to oxidation after the sample was removed from the furnace. For quantification, we ignore O and find that the whisker contains 17 wt% Ni as well as 2 wt% P (Supplemental[1]

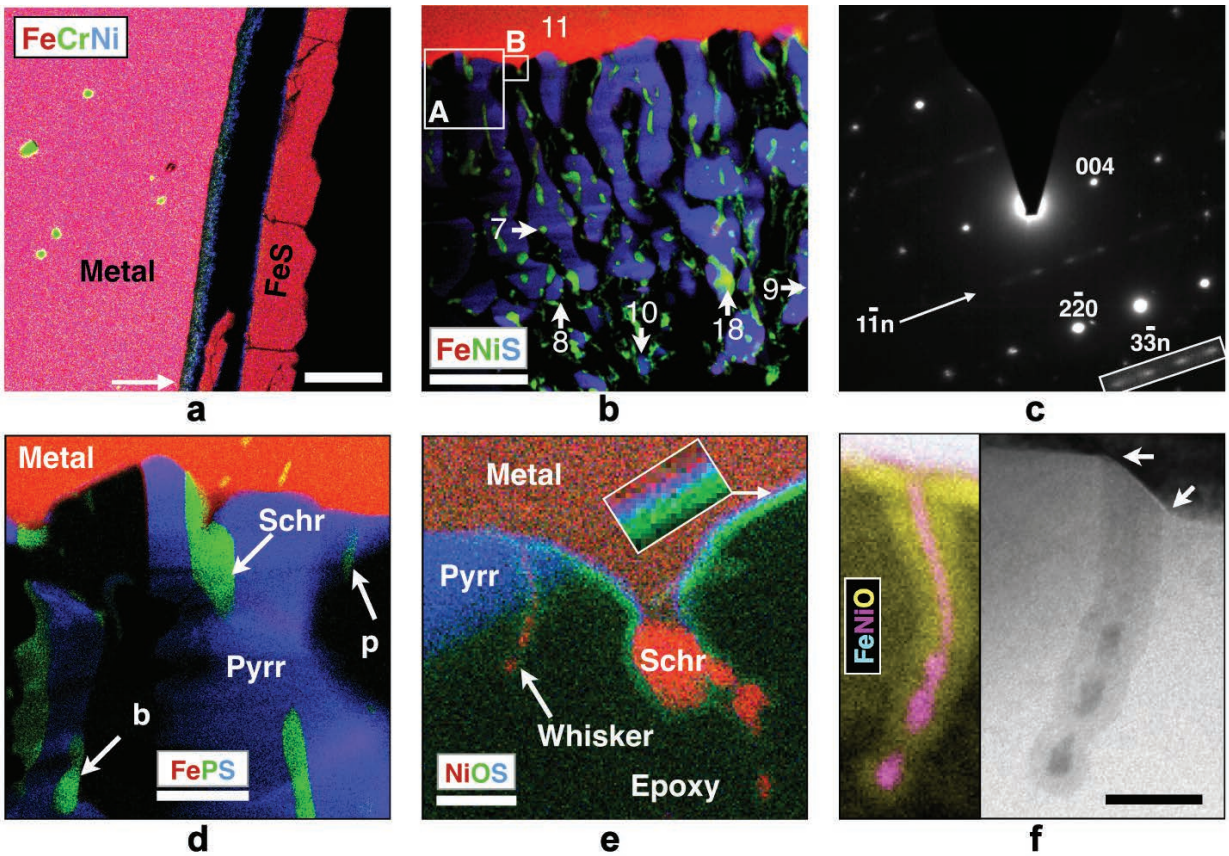

FIGURE 4. (**a**) SEM/EDS map taken at 20 keV of the 500 °C foil. The image is an LRGB image showing BSE (luminosity), Fe (red), Cr (green), Ni (blue). The metal and troilite appear red while the fine-grained material also containing schreibersite is blue. Chromite inclusions in the metal are green. The arrow indicates where the FIB lamellae were cut. The scale bar is 20 µm. (**b**) TEM/EDS map of one FIB lamella with Fe (red, metal), Ni (green, phosphide), and S (blue, sulfide). Embedding epoxy is black. Arrows indicate grains discussed in the text and are numbered according to Supplemental[1] Table 2. Region A is expanded in **d**; region B is expanded in **e**. (**c**) Selected area electron diffraction of pyrrhotite 4*C* (**b** spot 9 and Supplemental[1] Table 2, TEM 09) down the 110 zone. The $3\bar{3}n$ superlattice reflections are enhanced for visibility and plotted in Figure 8. (**d**) EDS map of the metal/sulfide interface. Fe (red), P (green), S (blue). Phosphide is green, sulfide is blue, and kamacite red; phosphorus-rich needles are yellow. Schr indicates schreibersite, Pyrr indicates pyrrhotite, b indicates barringerite, p indicates perryite, 200 nm scale bar. (**e**) EDS map showing a whisker (left) proximal to a forming phosphide (Schr, bright red) and the sequence of S (blue), and O (green) layers on the metal (light red). A neighboring pyrrhotite is labeled Pyrr. Ni is red, O is green, and S is blue. Scale bar is 50 nm. (**f**) Left: EDS map of a Ni-rich whisker (impurity region). Fe (cyan), Ni (magenta), O (yellow). Right: BF TEM image. Two arrows show that the slope of the metal changes on either side of the whisker. The scale bar is 25 nm.

Table 2, TEM 17). Other Ni-rich metals are also present as blebs away from the metal surface. For example, the bleb quantified in Supplemental[1] Table 2 TEM 18 has a taenite composition. In contrast to the whisker, the bleb is rich in sulfur rather than phosphorus and rounded rather than acicular.

Figure 5 shows the interrelationship between subgrain boundaries in the metal and sulfide/phosphide formation. Electron diffraction shows that all subgrain boundaries in the metal are oriented within a few degrees of each other. Phosphides can be seen growing from each of the bigger subgrain boundaries indicating that these are preferential growth sites for phosphide. Away from the subgrain boundaries, the phosphides tend to form on metal plateaus, usually surrounded by sulfide. The presence of Ni-rich regions can also be seen inside the metal, and high-resolution maps suggest that some phosphides are present in the metal at the grain boundaries.

The larger sulfide crystals usually grow from slight recesses in the Fe metal (compare Figs. 4b, 4d, 4e, and 5). The sulfide exhibits variable orientation partially in agreement with the XRD. In some cases, electron diffraction shows epitaxial metal/sulfide interfaces. Within tendrils, sulfide domains sometimes have similar orientations varying by only about 10° from each other, while other sulfide domains have orientations that are not clearly related to their neighbors. At the base of some tendrils, the sulfide/metal surface is littered with nano-polycrystalline sulfide (grain diameter ~10 nm). We will call this NPS. Fourier transforms of high-resolution images show varying degrees of order in the NPS ranging from a few overlapping crystalline patterns within the thickness of the FIB section to polycrystals with full rings. The former would have crystal domains tens of nanometers across while the latter would require crystal domains only a few nanometers across.

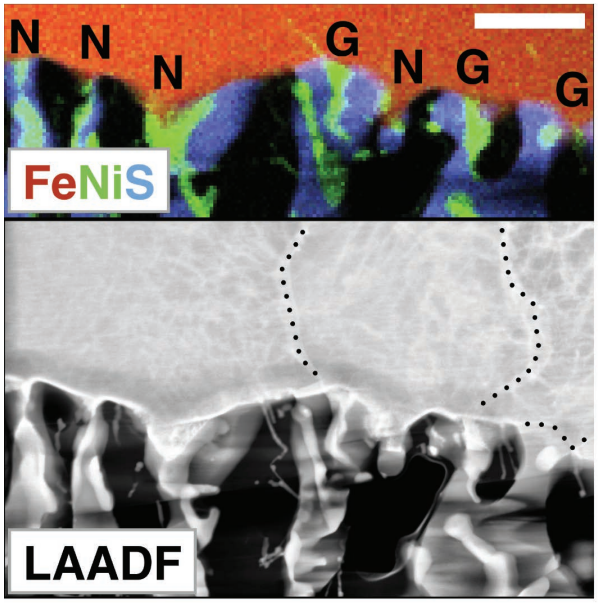

FIGURE 5. EDS map (**top**) of metal/sulfide interface from a second FIB section with Fe (red), P (green), S (blue). Low angle annular dark-field image (**bottom**) showing subgrain boundaries in the metal. Large subgrains are marked with dotted lines, and nano-subgrains can be seen by contrast. Phosphides growing out of subgrain boundaries are marked G, and phosphides not growing from subgrain boundaries are marked N. The scale bar is 1 μm.

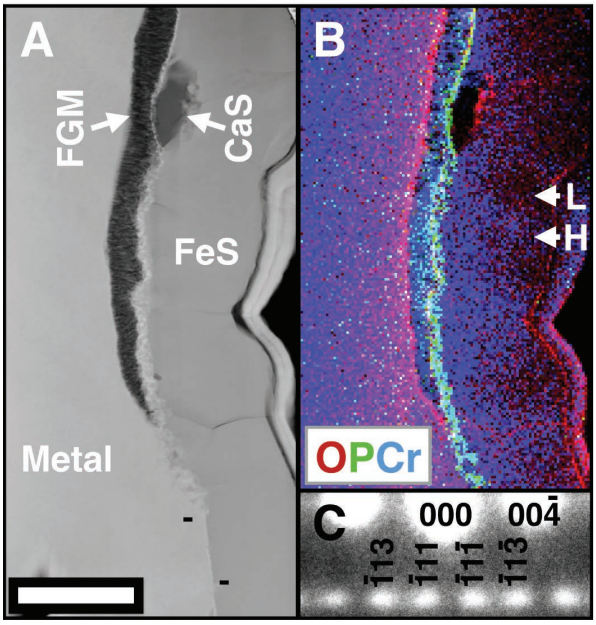

FIGURE 6. (**a**) HAADF STEM image of a FIB section from the foil sulfidized at 400 °C. FGM is a fine-grained mixture of FeS, Cr-rich sulfide, and phosphide. Scale bar is 2 μm. (**b**) EDS map of the same region with O (red), P (green), and Cr (blue) showing oxygen along grain boundaries in the FeS and at the metal surface, and inhomgeneity of Cr in the FeS. H represents a region of high-Cr concentration in the sulfide, L is low Cr. (**c**) Energy-filtered SAED pattern down the 110 zone axis showing very faint and diffuse 4*C* reflections (e.g., 113 and 113).

400 °C foil

Our final foil was sulfidized at 400 °C and shows a similar morphology to the foil sulfidized at 500 °C. In comparison to the 500 °C foil, this foil has a thinner sandwich of nanophases, and smaller crystallite sizes. Figure 6a is a HAADF STEM image of the interface. At the top, fine-grained material (FGM) can be seen sandwiched between metal and tabular sulfide (Supplemental[1] Table 3, spectra TEM 23, 24, and 19). At the bottom of the image, the tabular sulfide is still in direct contact with the metal. An oldhamite grain (CaS) is present at the interface (Supplemental[1] Table 3, TEM 22). Figure 6b shows that Cr is inhomogenous in the tabular sulfide ranging from as high as 0.7 wt% to as low as 0.3 wt% (Supplemental[1] Table 3, TEM 20 and 21). Cr is highest close to the metal, and quickly drops off with distance from the metal. Concentration of Cr is also higher along grain boundaries in the sulfide, and in the FGM. The EDS image shows that the FGM has two layers. The layer closest to the metal is dominated by Cr-rich sulfide with a some phosphide. The layer closest to the tabular sulfide is dominated by phosphide with some Cr-sulfide. Ni is enriched by only a few percent in the metal surface closest to the FGM. Figure 6c shows an energy-filtered diffraction pattern of a tabular sulfide showing diffuse 4*C* (11*n*) reflections indicating the formation of pyrrhotite rather than troilite.

Impurity regions

We see the presence of "impurity regions." These are metal zones that are significantly enriched in Ni, P, Co, Cu, and Si, elements that are more siderophile than chalcophile under the sulfidation conditions. The name is motivated by the idea that any and all elements left behind by the sulfidation reaction will be concentrated into a reservoir whose crystal structure may change to accommodate the hodge-podge of elements. Impurity regions often have an FCC crystal structure compared to the BCC bulk metal and tend to occur on grain boundaries. In the limiting case, all the metal would be consumed and "pure" sulfide would be surrounded by "impure" regions containing all the sulfide-incompatible elements. In practice impurity regions probably nucleate other phases such as schreibersite before reaching such a limit, as discussed shortly.

In the 900 °C foil, the impurity region is several micrometers thick and contains taenite near the metal sulfide interface due to the enrichment of Ni. In the 500 °C foil, the impurity regions are much smaller, and located as outcroppings or whiskers extending beyond the metal surface, or detached from the metal some micrometers away from the surface. The whisker in Figure 4f is one such impurity region enriched in Ni, P, and Si (Supplemental[1] Table 2, TEM 17). Spectrum TEM 18 in Supplemental[1] Table 2 shows another impurity region detached from the metal/sulfide interface, which is enriched in Ni and Co.

Careful examination shows that the features of the metal surface are frequently bounded by impurity regions. The change in the slope of the metal surface at each edge of the whisker shown in Figure 4f is one example. Figure 4b shows several more locations where the morphology of the metal surface changes with the presence of sulfide and schreibersite.

Discussion

We can make several useful comments about the formation of sulfide under the conditions of this experiment. Our purpose is to put forth a model for the sulfide growth that will facilitate thinking about disequilibrium sulfide growth and to provide several key observables that future researchers can measure in astromaterials to link (or not) their results with this experiment. We will also discuss where future work needs to be done.

Diffusion in pyrrhotite

Condit et al. (1974) measured diffusion of Fe and S in pyrrhotite ($Fe_{1-\delta}S$, $0 \leq \delta \leq 0.125$) and found that the rate of diffusion for Fe is approximately four orders of magnitude faster than sulfur, and occurs via a vacancy diffusion mechanism. The diffusion rate can be an order of magnitude faster than in pure troilite and depends on the temperature and δ with the fastest iron diffusion near $\delta = 0.07$ (685 K). At higher temperatures, the diffusion maximum occurs at larger δ. Diffusion along the *c* axis of pyrrhotite is 1.8 times faster than along the *a* axis.

The 1*C* ↔ 2*C* transition temperature above which iron sulfide has the NiAs (1*C*) unit cell and below which it has the 2*C* unit cell is 315 °C (Wang and Salveson 2005). The many pyrrhotite superlattices that exist at lower temperatures are not present above the transition temperature. This implies that most pyrrhotite formation occurs without any superlattice, and the superlattice only forms during the final stages of the process as the sample cools. This is true in our experiment, too; all foils were reacted above the 1*C* ↔ 2*C* transition temperature. The superlattices we see were formed during rapid quench and reflect the freezing in of the initial composition. Assuming the quench was sufficiently fast to prevent further segregation into pyrrhotite and troilite, the δ we observe should be the same as the δ for the 1*C* sulfide.

In understanding the sulfidation layers, we have to consider the sulfur as relatively immobile, reacting primarily near the gas-sulfide surface, while Fe atoms diffuse easily. In diffusion-limited disequilibrium conditions, we propose that non-stoichiometric iron sulfide is favorable over troilite because of the higher diffusion rate of Fe in non-stoichiometric iron sulfide. Ni diffusion kinetics are thought to be similar to Fe since NiS forms similar structures and substitutes as a solid solution with Fe (Condit et al. 1974).

Iron structure

The Fe-Ni phase diagram (Swartzendruber et al. 1991) indicates that Fe has a BCC structure (space group $Im\bar{3}m$) except at temperatures above 912 °C or when a few percents of Ni is dissolved into the structure, at which point it assumes an FCC structure (space group $Fm\bar{3}m$). The presence of P in the metal tends to stabilize the BCC structure and promote the nucleation of phosphides. Based on the expanded Fe-Ni-P phase diagram (Doan and Goldstein 1970) we expect the foil sulfidized at 900 °C began in a two-phase region with BCC and FCC Fe connected by a tie line. As the foil sulfidized, we saw that the metal became more Ni-rich and it would have moved to a two-phase region with FCC Fe and phosphide. However, as the metal cooled, the residual P in the metal would have promoted nucleation of BCC Fe domains (Doan and Goldstein 1970).

Based on the Fe-Ni-P phase diagram of Doan and Goldstein (1970) the bulk foils sulfidized at 500 and 400 °C began in a two phase region with BCC Fe and phosphide. After some Ni enrichment the system entered a three-phase region with BCC and FCC Fe as well as phosphide.

As Ni was the most concentrated element in impurity regions, it follows that impurity regions were FCC iron, whereas the bulk metals were BCC (except possibly for the foil sulfidized at 900 °C).

Growth model

Based on the sulfide morphologies we observed in these samples, and the relative positions of all phases, we propose a model for the formation of the sulfide, schreibersite, and other phases.

During initial sulfidation, sulfide grows rapdily in the linear growth regime noted by Lauretta (2005) until it forms a compact surface and inhibits diffusion of S to the metal. After this point, there are two reaction surfaces: the sulfide/H_2S interface will consume sulfur from the gas phase and the metal/sulfide interface will consume Fe from the metal surface. At this time, Fe diffusion outward becomes important as it must constantly supply Fe through the entire sulfide layer to the sulfide/H_2S interface. This is the onset of the parabolic diffusion limited regime described by Lauretta (2005), and is why pyrrhotite becomes the dominant sulfide. Pyrrhotite is not thermodynamically more stable than troilite, but it is dynamically more stable since it supports the diffusion of Fe from the metal/sulfide interface to the sulfide/gas interface. The diffusion of Fe atoms outward from the metal/sulfide interface leaves a deficit of material at the metal/sulfide interface and conservation of mass requires that the metal volume diminish. It may be that the tendril structure we see reflects this mass loss.

Figure 7 schematically gives a more detailed look at the process. We propose that the initial nano-polycrystalline sulfide (NPS) growth covers the surface of the metal. Subsequent Ostwald ripening causes a few of the nanocrystals to grow at the expense of other nanocrystals. Initially S is abundant and the largest crystals grow rapidly across the surface leaving the surrounding metal concentrated in siderophile elements resulting in impurity regions rich in Ni, Co, P, and Si. These steps are shown in Figure 7, frames i and ii where the sulfide (blue) nucleates on the surface of the metal (red) and causes impurity regions (yellow). Eventually the sulfide incompatible elements in the impurity region become so concentrated as to inhibit further lateral growth of the sulfide and cause it to grow perpendicular to the metal surface. Grain boundaries are also known to concentrate impurities such as P in Fe metal (Erhart and Grabke 2013), and therefore lateral sulfide growth will frequently end at grain boundaries. At high temperatures (such as with the 900 °C foil), the Fe metal has an FCC structure and nickel enrichment can proceed continuously as any concentration of Ni is allowed. At low temperatures (such as with the 500 and 400 °C foils) the Fe metal remains in a BCC structure until Ni enrichment forces the transition to the FCC (taenite) structure. Therefore impurity regions have a different crystal structure compared to the bulk metal, and this facilitates elemental segregation. These impurity regions act as nucleation sites for phases such as schreibersite, perryite, etc., or remain as taenite. Schreibersite can also nucle-

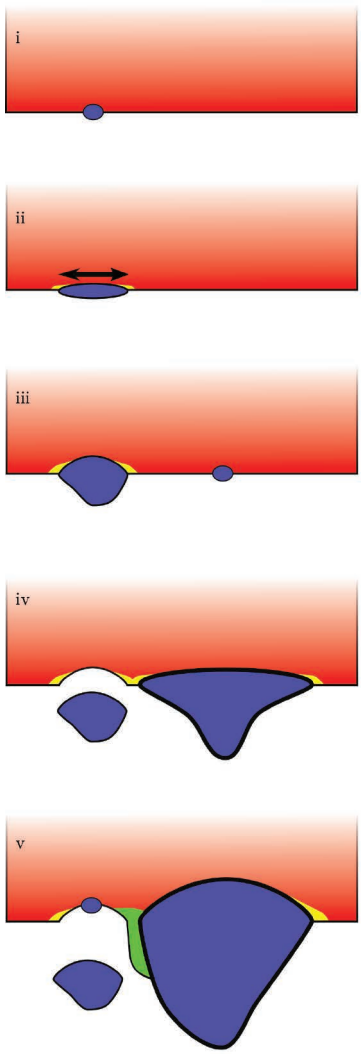

FIGURE 7. Schematic of a proposed model for the formation of the sulfide discussed in the growth model section. Red is Fe metal. Blue is sulfide. Yellow are impurity regions (see text). Green is schreibersite.

ate beneath the surface of the metal (Erhart and Grabke 2013) and grow rapidly once sulfide growth exposes it. Vertical sulfide growth forms tendrils with ever widening bases until neighboring tendrils touch and the impurity regions at their boundaries combine to create plateaus. Occasionally, sulfide crystals detach from the metal exposing fresh surface and the sequence repeats with the formation of NPS on the new surface. Figure 7, frame iii shows competing grains growing, and frame iv shows them touching at the bases and forming an impurity plateau. One of the sulfide crystals detaches by chance. Eventually, other phases such as schreibersite, and barringerite can nucleate on these plateaus when Ni, P, or Si become highly concentrated. This is shown in Figure 7, frame v as the green phase. After nucleation of alternate phases, the "impurity" phase will now grow actively through the crystal growth dynamics that govern that phase. Figure 7, frame v demonstrates this as the green phase rapidly develops perpendicular to the metal and along the lateral surface of the sulfide, as we observe with schreibersite in the experimental foils. Once an impurity phase such as schreibersite nucleates, it will act as a sink for impurity elements and will inhibit growth of the same impurity phase in the immediate vicinity.

The sulfide/schreibersite morphologies shown in Figures 4 and 5 are the basis our model. We see that schreibersite forms on the metal ridges and grain boundaries. The composition of the whisker in Figure 4f is intermediate between Ni-rich metal and schreibersite. We postulate that this is simply an impurity region that has become concentrated in the elements that favor schreibersite production, but where schreibersite has not yet nucleated. The metal with taenite composition seen in Figure 4b, spot 18 (Supplemental[1] Table 2, TEM 18) was rich in Ni, Co, and S but not P. It is surrounded by phosphide grains so this is an impurity region that was enriched in Ni and P initially, but the P has been lost to neighboring phosphide grains and remained as taenite. In the case of the 900 °C foil, the diffusion of elements is sufficiently fast so that impurity regions are large and spaced far apart. When schreibersite does nucleate, P can diffuse to the schreibersite from several micrometers away and support its growth so we see coarse-grained phosphide. At 500 °C impurity regions are only a few nanometers in size and diffusion only operates on a length scale of hundreds of nanometers. The impurity regions nucleate separately to produce a rich diversity of phases. At 400 °C, diffusion is very slow and the impurity elements become trapped exactly at the metal/sulfide interface.

Equilibrium and partition coefficients

Experimental partition coefficients for the foils sulfidized at 900, 500, and 400 °C are in Supplemental[1] Table 4 as:

$$D^{\text{element}}_{\text{phase}} = D^{\text{element/Fe}}_{\text{metal/phase}} = \frac{X^{\text{El}}_{\text{metal}} / X^{\text{Fe}}_{\text{metal}}}{X^{\text{El}}_{\text{phase}} / X^{\text{Fe}}_{\text{phase}}}$$

where $X^{\text{Fe}}_{\text{metal}}$ is the abundance of Ni, Cr, or P in the metal, and similarly for X_{phase} where phase is either troilite, pyrrhotite, pentlandite, or daubréelite.

For the foil sulfidized at 900 °C, we computed "pseudo-equilibrium troilite" values from Lauretta (2005) Table 1, and they represent the closest approach to equilibrium between the sulfide and metal phase. Since elemental zoning is present and the reaction was interrupted before completion, these are not actual equilibrium values. The "troilite at interface" values are from the FIB section (Fig. 2b) and compares the least Ni-rich kamacite metal (spot 5), against the sulfide closest to it (spot 2). D^{Ni} is 13× greater than the pseudo-equilibrium partition, which indicates that the Ni is highly concentrated in the metal near the metal/sulfide interface. D^{Cr} is the opposite indicating that Cr is accepted into the sulfide and depleted in the metal at the interface. Phosphorus is below detection limits in the sulfide. This is similar to the trends shown in the line scan in Figure 2d.

The foil sulfidized at 500 °C shows a more detailed story. Again, "pseudo-equilibrium troilite" is the closest approach to equilibrium based on Lauretta (2005). "Tabular pyrrhotite" is the average of spectra TEM 15 and 16 in Supplemental[1] Table 2 from the coarse-grained sulfide layer and based on our growth model should be closer to equilibrium than the "tendril pyrrhotite"

located in the fine-grained region. We see that D^{Ni} and D^{Cr} are higher for more equilibrated pyrrhotite and therefore, Ni and Cr both partition preferentially into disequilibrium pyrrhotite if they both formed at the same temperature. The schreibersite crystals do not contain measurable Cr, but the Ni behaves opposite to pyrrhotite, namely Ni is more concentrated in equilibrium crystals compared to disequilibrium crystals. However, we have no evaluation of the pseudo-equilibrium schreibersite partition so we cannot define a trend.

We see up to 0.4 wt% P in the sulfide tendrils though P was below detection in the larger sulfide crystals and in the microprobe studies. It is unlikely that P is actually present in the sulfide lattice, instead nanoscale schreibersite leads to the spurious detection of P in the sulfide via electron scattering. Nevertheless, nanoscale schreibersite would be difficult to detect in HRSEM, and impossible to see in microprobe and would lead to the apparent detection of P in the sulfide by EDS and WDS. Therefore, detection of P in sulfide can be used as an indicator of disequilibrium formation.

The foil sulfidized at 400 °C shows inhomogeneity of Cr. Therefore, there is not a single partition value, but a range. The length scale of inhomogeneity is on the order of a micrometer and should be accessible to low-voltage SEM or FE-probe EDS/WDS measurements. Essentially all the Ni and P, and much of the Cr is captured in the fine-grained region. In an SEM or probe view, this could be distinguished as a spike in Ni, P, and Cr concentration at the metal/sulfide interface. A complication in using partition coefficients for sulfide arises from the fact that it shows different trends as a function of temperature and equilibrium. Consider D^{Ni} where the pseudo-equilibirum value increases from 1.85 at 900 °C through 2.32 at 500 °C, to 6.72 at 400 °C. Therefore, Ni partitions into pyrrhotite more favorably at higher temperatures. However, at 500 °C, we see the equilibrated pyrrhotite (pseudo-equilibrium and tabular are similar) has $D^{Ni} \approx 2.4$, but the disequilibrated, tendril pyrrhotite has $D^{Ni} = 1.62$. Therefore one would expect a competition between temperature and equilibrium: high temperature and disequilibrium both favor more Ni in the pyrrhotite. It will be important to consider other indicators of equilibrium alongside chemical composition to unravel the formation history of a natural sulfide.

Superlattice vs. equilibrium

As pyrrhotite becomes disordered, superlattice reflections become weaker and more diffuse. Harries et al. (2011) discuss streaking in the diffraction pattern as arising from mesoscopic disorder and noticed it in an *nC* pyrrhotite from Nyseter mining area, near Grua, Norway. Nakazawa and Morimoto (1971) noticed streaking in synthetic pyrrhotites with $\delta < 0.1$ that had been "equilibrated" at temperatures <400 K. This suggests that superlattice disorder may be an indicator of disequilibrium and/or low-temperature formation.

To put this on a quantitative footing, we analyzed the broadening of superlattice peaks in SAED patterns using methods derived from the X-ray diffraction community. First, we note that the full-width at half maximum (FWHM) of a peak is a function of three major factors: (1) The electron optics and the spread in energies of the e-beam cause reflections to have a minimum width regardless of the crystal being studied. We call this the instrument response (H_I). (2) A specific crystal is expected to have a calculable peak width even if it is perfect. Nanocrystals have more diffuse reflections compared to infinite crystals due to their finite size. Low angle inelastic scattering in the electron beam broadens SAED reflections and is a function of the thickness and density of the crystal. Energy filtered imaging can eliminate the latter effect. We bundle all contributions expected for a perfect crystal into the crystal response (H_C). (3) Finally, crystal disorder in the form of internal strain and defects broadens the reflections. It is this final contribution we are interested in, and we call it the disorder response (H_D). For more information about the physics behind instrument, crystal, and disorder broadening in diffraction see Cullity and Stock (1978).

We define a primary reflection as a reflection in the SAED pattern that would be present if the sample was troilite (i.e., devoid of any superlattice). We then make an approximation that the primary reflections have no disorder, which implies that broadening of the primary reflections is due only to H_I and H_C above. We compare the FWHM of a superlattice reflection to a primary reflection and any difference in the FWHM is due to disorder of the superlattice, H_D. It is known that if one uses a Lorentzian (Cauchy) distribution to fit a diffraction reflection, then the broadening contributions can be subtracted off linearly (Balzar 1999). For example, if a primary reflection has a FWHM of 0.1 nm^{-1} in the SAED, and the superlattice reflection has a FWHM of 0.3 nm^{-1} then the contribution from disorder is 0.2 nm^{-1}.

Figure 4c shows an electron diffraction pattern acquired down the 110 zone of pyrrhotite from the 500 °C foil. The reflection labeled $2\bar{2}0$ is a primary reflection and has a FWHM of 0.07 nm^{-1}. The box highlights a row of superlattice reflections from $3\bar{3}1$ to $3\bar{3}7$ with peak centroids located in the positions expected for pyrrhotite 4*C*. Ideal pyrrhotite 4*C* would have symmetric superlattice reflections with the same FWHM as the primary reflection but these reflections are asymmetric and

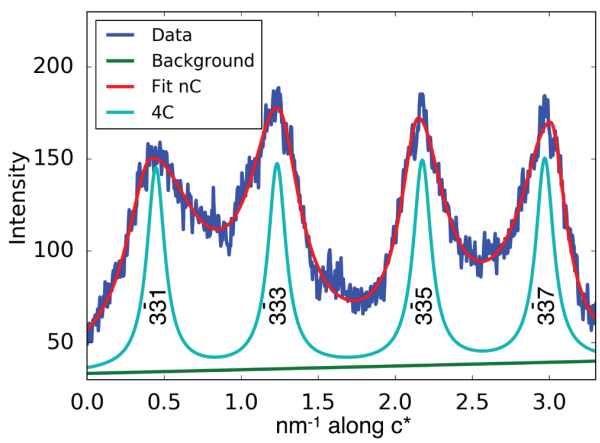

FIGURE 8. Fit of the pyrrhotite superlattice peaks highlighted in Figure 4c, which is from the crystal marked as spot 9 in Figure 4b. A linear background is subtracted in both cases. "Fit *nC*" shows a fit using asymmetric Lorentzians (see text), while "4*C*" uses symmetric Lorentzians with the width of the primary reflections.

have a broader FWHM. Figure 8 shows a fit against the $3\bar{3}1$ to $3\bar{3}7$ peaks highlighted in Figure 4c, plotted in the crystal direction c*. The experimental intensities are shown in dark blue, and a linear background is subtracted from the fits. We fit the peaks using split-Lorentzian functions (Wojdyr 2010) and find the FWHM is ≈5× the FWHM of the primary reflection in the same pattern. This fit demonstrates the presence of periodicities other than 4*C*, but the lack of well-defined *nC* reflections indicates these structures are disordered. They could perhaps be considered *nC* structures where *n* is not a single value. Since the sulfide in the experimental run is heterogeneous, it must be out of equilibrium. Therefore, we have shown that a disequilibrium sulfide may have a disordered superlattice, and we have a potential quantitative measure for it.

Supplemental[1] Table 5 shows several similar measurements for comparison. Measurements A1 and A2 are from a SAED pattern of Chihuahua pyrrhotite 4*C* taken down the 110 zone axis from a FIB section. Using the 11*n* and 33*n* series of superlattice reflections normalized against the 22*n* primary peaks, we find that there is no measurable peak broadening, and hence no disorder. This is a control case for our approach. Meaurements B1 and B2 are from the edge of same FIB section, where there is some ion damage to the crystal. The disorder broadening is now 0.005 nm^{-1}. The broadening due to crystallite size and instrumental factors in this SAED pattern is 0.06 nm^{-1}. This demonstrates that we can resolve disorder broadening an order of magnitude smaller than the broadening from instrumental factors or crystallite size. Measurement C1 shows the broadening from a tabular (more equilibrated) pyrrhotite in the 500 °C foil. The broadening is now 0.2 nm^{-1}, significantly larger than instrumental/crystal size factors. Measurements D1 and D2 show measurements from a tendril sulfide (less equilibrated) which average 0.31 nm^{-1}. The difference between the two measurements is now 0.06 nm^{-1} (standard deviation 0.03 nm^{-1}), so in disordered samples, the broadening is sensitive to which reflection is used to measure disorder. This is expected based on diffraction theory (Cullity and Stock 1978; Balzar et al. 2004; Williamson and Hall 1953) Measurements E1–E6 show 6 measurements of a tendril sulfide (less equilibrated) using different combinations of superlattice and primary reflections, but on a different microscope and with an energy filter. The average disorder broadening is 0.34 nm^{-1}, and the standard deviation is 0.02 nm^{-1}, which is better than for the unfiltered case. This demonstrates two facts: (1) our approach is reproducible across different instruments with reasonable accuracy; (2) energy-filtered patterns will provide better results. Measurements F1 and F2 are from a tendril sulfide but along a different zone axis. The integration direction is along a*, orthogonal to c* and therefore sampling a different component of the crystal disorder. To compare results, one should use the same zone axis and integration direction. Measurement G1 is from a tabular (more equilibrated) sulfide in the 400 °C foil. It has more disorder broadening than the 500 °C sulfide. Therefore, we expect the disorder to increase with decreasing formation temperature of the sulfide, all other factors held constant (f_{S_2}, time, pressure, composition).

For future comparisons, we encourage researchers to use the 110 zone axis, integration in the c* direction, and energy-filtered images. Obviously, if disorder in a different crystallographic direction is of interest, then different superlattice reflections and integration directions must be chosen, but the researcher should be aware then that his disorder broadening may not directly compare to our numbers.

Crystal orientation

Lauretta et al. (1996) found pyrrhotite grains grew with various orientations on Fe metal and the orientation varied as a function of sulfur fugacity and temperature. Narita and Nishida (1973) found that pyrrhotite growing from Fe-Cr metal at high f_{S_2} grew with with the *c* axis perpendicular to the metal surface. Figure 9 shows the histogram of the crystal orientations in Figures 1c and 3b. The sulfide crystals from the foil sulfidized at 900 °C are preferentially oriented at 90° meaning that the troilite *c* axis is in the plane of the metal-sulfide interface. The mean value is 87° (σ = 20°), meaning that more than 95% of the crystals are within 40° of this orientation. On the other hand, sulfide sulfidized at 500 °C shows a preference for an out of plane orientation of 30° (σ = 12°).

HRTEM imaging shows that preferential orientations do occur, but the process governing the orientations is not one-to-one; some tendrils show relationships that other tendrils do not.

There may be two different growth regimes observed in our samples. In the foil sulfidized at 500 °C, we occasionally observed epitaxial growth of the sulfide on the Fe metal with HRTEM. Nearby regions on the same foil exhibited the NPS layer, which was not epitaxial. Larger crystals had variable orientations, though the orientations were not entirely random. It is not possible to explain all orientations as a simple epitaxial relationship to the metal and yet there are clearly preferential orientation directions that depend on temperature.

Minor phases forming alongside sulfide

The primary phases we saw were metal, chromite (already present in the metal), pyrrhotite, and schreibersite. We also saw

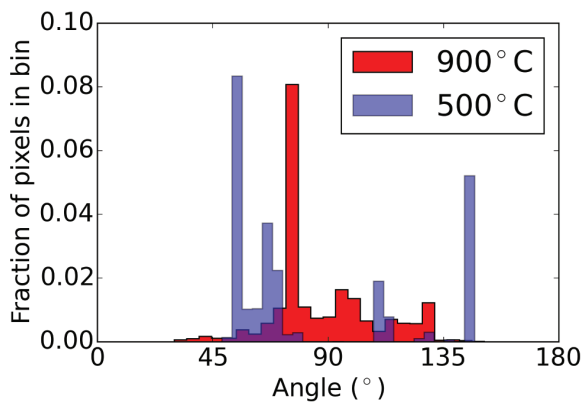

FIGURE 9. Histogram of the sulfide/metal angles measured by μXRD from the foils sulfidized at 900 °C (red) and 500 °C (blue). An angle of 90° means the *c* axis of the sulfide is normal to the metal surface (i.e., in the plane of the metal surface). 0° means it is colinear pointing up from the metal, and 180° means it is pointing down into the metal.

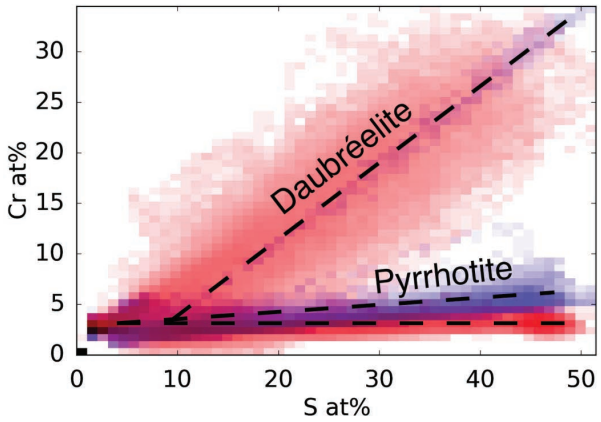

Figure 10. Element correlation plots for Cr vs. S in 400 °C (red) and 500 °C foils (blue). The data have been corrected for a thin film absorption through troilite.

daubréelite, barringerite, oldhamite, and a phase close to perryite. We did not see pentlandite, which is frequently seen in astromaterials. These phases are occasionally seen in extraterrestrial samples such as meteorites and interplanetary dust particles. Therefore, they are of interest insofar as they may be produced by the same disequilibrium processes that can create pyrrhotite.

We will first discuss daubréelite. A correlation plot is shown in Figure 10 displaying the abundance of Cr vs. S for each pixel in EDS maps of both the 400 °C (red) and 500 °C foils (blue). A thickness correction of 100 nm with a density of troilite (4.69 g/cm^3) was applied to each pixel. Two different correlations are visible in each map. The bottom branch leading from the origin to ~50 at% S and 2–5 at% Cr corresponds to the pyrrhotite phase. The Cr partitions less favorably into the pyrrhotite in the 400 °C foil, and instead forms Cr-rich sulfide (upper branch), the end-member of which is daubréelite. However, while the pyrrhotite phases appear homogenous in both foils, the daubréelite is much less homogenous in the low temperature foil as seen by the dispersion in EDS data, and more abundant as seen in the fraction of pixels in the daubréelite branch. Therefore, it seems that daubréelite is thermodynamically more favorable at low sulfidation temperatures and forms as an accessory phase. The presence of daubréelite in combination with the Cr zoning seen in the 400 °C foil may explain the unusually high activity coefficients determined by Lauretta (2005) for CrS in the sulfide since they were unable to identify the Cr carrier phase using microprobe analysis.

Co and Si are both siderophile under these formation conditions and concentrate into impurity regions like P. Therefore, barringerite (Co-rich phosphide) and perryite (Si-rich phosphide) probably form similarly to schreibersite.

We saw oldhamite in the 400 °C foil at the interface between the troilite and fine-grained material. It was inset into the tabular pyrrhotite. Ca is a lithophile element so it is not clear whether it formed from a Ca-rich inclusion in the metal or if it nucleated later. Oldhamite is formed at high f_{S_2} and low f_{O_2} such that it would not normally form under the conditions of the canonical solar nebula (Larimer 1968), but it is found in enstatite chondrites alongside daubréelite, schreibersite, perryite, and other reduced phases (Lehner et al. 2010; Jacquet et al. 2015). Assemblages of these phases indicate complicated histories.

Pentlandite is absent in our experimental assemblages. Etschmann et al. (2004) found that pentlandite rapidly exsolves from pyrrhotite/troilite at temperatures >200 °C, even in <1 h, whereas our experiments were carried out at temperatures ≥400 °C and for 4.5 h. Etschmann et al. (2004) also noted that high sulfur fugacities and concentrations of elements other than Fe or Ni in the sulfide both suppress the rate of exsolution of pentlandite. Lauretta et al. (1997) found that they produced pentlandite from gas phase sulfidation of Canyon Diablo metal using 50 ppm H_2S in H_2 in contrast with the 1.1% H_2S in the experiments described here (Lauretta 2005). Therefore, f_{S_2} is ~2–3 log units lower in the foils that produced pentlandite. In addition, Canyon Diablo kamacite contains a few wt% Ni and P, but other elements are in the parts per million range. Therefore, the compositional difference could be a significant suppressor of pentlandite.

Application to IDPs, Wild 2, and meteorites

These experiments were intended as analogs for sulfide formation in the solar nebula. Some of the published work on cometary and asteroidal samples contains offhand or incidental observations, which can better be interpreted in light of our work or provides avenues for future analysis.

P-bearing sulfide is rarely reported, but has occasionally been seen. Lauretta and Buseck (2003) examined 10 chondrules in Bishunpur and compared grains within the chondrules to those exposed to the nebular environment at the edges of the chondrules with only minor evidence of parent body effects. P concentrations up to 0.47 wt% were seen but only in the sulfide on the periphery of the chondrules, presumably exposed to the nebula. Since their analysis used a microprobe they were not able to distinguish between P present in nano-phosphides vs. P residing in the sulfide lattice. We interpret the P as an indicator of disequilibrium in the formation of the sulfides during the nebular process.

nC pyrrhotite has been noted in interplanetary dust particles and Wild 2 comet samples by several researchers including Christoffersen and Buseck (1986), Dai and Bradley (2001), and Gainsforth et al. (2014). At present, the diffuse reflections in the literature only qualitatively indicate that at least some sulfides present in IDPs probably formed out of equilibrium. However, Dai and Bradley (2001) and Gainsforth et al. (2014) show euhedral nano-pyrrhotites with diameters on the order of 100 nm with disorder to the extent that superlattice spots become bands with a boxcar profile. Compositional zoning in the Wild 2 cometary sulfide reported by Gainsforth et al. (2014) indicate that it formed under diffusion limited conditions yet it shows no evidence of coexisting with another phase, has a carbonaceous rim, and a phosphorus hot spot—all that seem to indicate a process like nebular sulfidation. We hypothesize that such sulfides may be characteristic of another low-temperature sulfidation regime, perhaps even below the NiAs transition temperature at 315 °C. Such low temperatures are difficult to execute in a laboratory setting, but an experiment exposing Fe nanoparticles at low temperature should be possible in the laboratory and may prove or disprove this hypothesis.

Mackinnon and Rietmeijer (1987) report a CP-IDP with daubréelite. Without compositional information and petrographic context, the meaning is unclear but if daubréelite is found in future IDPs, then its relationship with the neighboring sulfide and phosphide can be explored within the context of nebular sulfidation using our partition coefficients and sulfidation model.

There have been many studies of pyrrhotite in meteorites that experienced other forms of disequilibrium formation such as aqueous processing or retrograde metamorphism (e.g., Bullock et al. 2005; Zhang et al. 2008; Harries and Langenhorst 2013; Berger et al. 2016). SAED patterns shown in these papers sometimes show broadening of superlattice reflections. The FWHM method may have a more general application to meteorites and even to geological samples, though quantitative interpretation will only be possible after diffraction data are made available either from more samples or aqueous analog experiments.

Implications

Disequilibrium sulfide formation produces different phases under low f_{S_2} than equilibrium formation, which requires that all metal be consumed into troilite before pyrrhotite can form. In our experiment, disequilibrium conditions allowed metal and troilite to coexist with pyrrhotite, schreibersite, daubréelite, barringerite, oldhamite, and perryite. In addition to the surprising mineral assemblage, we found several observables that can be used to determine if sulfide formed out of equilibrium. P is incompatible in troilite/pyrrhotite but may still be present out of equilibrium as nano-phosphide in the sulfide. Cr was found to be inhomogeneous in sulfide formed at low temperatures. Electron diffraction patterns can have broader superlattice reflections when the sulfide formed out of equilibrium. We developed a superlattice disorder metric using a simple peak width analysis.

Cometary samples from comet Wild 2, interplanetary dust particles and meteorites contain sulfide thought to have formed via sulfidation of metal by H_2S gas in the early solar nebula as well as via other mechanisms. Extraterrestrial sulfides often show disordered superlattices, measurable P content, and nonstoichiometric compositions. Our work provides an explanation for these features: the sulfide may have formed out of equilibrium. This insight also provides a guide for future experiments that should attempt to sulfidize nano-phase Fe under low f_{S_2} at low temperatures.

Such experiments should target temperatures below troilite's magnetic transition at 315 °C since the diffusion characteristics are expected to change.

Acknowledgments

We thank our editor Rhian Jones, as well as Adrian Brearley and an anonymous reviewer for insightful evaluation of this paper. Their efforts significantly improved the quality of this work. The ALS and NCEM are supported by the Director, Office of Energy Research, Office of Basic Energy Sciences, Materials Sciences Division of the U.S. Department of Energy, under Contract No. DE-AC02-05CH11231.

References cited

Balzar, D. (1999) Voigt-function model in diffraction line-broadening analysis. International Union of Crystallography Monographs on Crystallography, 10, 94–126.

Balzar, D., Audebrand, N., Daymond, M., Fitch, A., Hewat, A., Langford, J., Bail, A.L., Louër, D., Masson, O., and McCowan, C. (2004) Size-strain line-broadening analysis of the ceria round-robin sample. Journal of Applied Crystallography, 37, 911–924.

Berger, E.L., Lauretta, D.S., Zega, T.J., and Keller, L.P. (2016) Heterogeneous histories of Ni-bearing pyrrhotite and pentlandite grains in the CI chondrites Orgueil and Alais. Meteoritics and Planetary Science, 51, 1813–1829.

Bullock, E., Gounelle, M., Lauretta, D., Grady, M., and Russell, S. (2005) Mineralogy and texture of Fe-Ni sulfides in CI1 chondrites: Clues to the extent of aqueous alteration on the CI1 parent body. Geochimica et Cosmochimica Acta, 69, 2687–2700.

Carlson, W.D., Pattison, D.R.M., and Caddick, M.J. (2015) Beyond the equilibrium paradigm: How consideration of kinetics enhances metamorphic interpretation. American Mineralogist, 100, 1659–1667.

Christoffersen, R., and Buseck, P.R. (1986) Mineralogy of interplanetary dust particles from the "olivine" infrared class. Earth and Planetary Science Letters, 78, 53–66.

Condit, R.H., Hobbins, R.R., and Birchenall, C.E. (1974) Self-diffusion of iron and sulfur in ferrous sulfide. Oxidation of Metals, 8, 409–455.

Cullity, B. and Stock, S. (1978) Elements of X-ray Diffraction, 2nd ed. Addison-Wesley, Reading, Massachusetts.

Dai, Z., and Bradley, J. (2001) Iron-nickel sulfides in anhydrous interplanetary dust particles. Geochimica et Cosmochimica Acta, 65, 3601–3612.

Davis, A.M., and Richter, F.M. (2005) Condensation and Evaporation of Solar System Materials. Elsevier.

de Villiers, J.P.R., and Liles, D.C. (2010) The crystal-structure and vacancy distribution in 6*C* pyrrhotite. American Mineralogist, 95, 148–152.

de Villiers, J.P.R., Liles, D.C., and Becker, M. (2009) The crystal structure of a naturally occurring 5*C* pyrrhotite from Sudbury, its chemistry, and vacancy distribution. American Mineralogist, 94, 1405–1410.

Doan, A.S., and Goldstein, J.I. (1970) The ternary phase diagram, Fe-Ni-P. Metallurgical Transactions, 1, 1759–1767.

Erhart, H., and Grabke, H.J. (2013) Equilibrium segregation of phosphorus at grain boundaries of Fe–P, Fe–C–P, Fe–Cr–P, and Fe–Cr–C–P alloys. Metal Science, 15, 401–408.

Etschmann, B., Pring, A., Putnis, A., Grguric, B.A., and Studer, A. (2004) A kinetic study of the exsolution of pentlandite (Ni, Fe)$_9$S$_8$ from the monosulfide solid solution (Fe, Ni)S. American Mineralogist, 89, 39–50.

Gainsforth, Z. (2016) Stoichiometry Fitter, a GUI for fitting solid solutions and analyzing mineral phases. Microscopy and Microanalysis, 22, 1808–1809.

Gainsforth, Z., Butterworth, A.L., Stodolna, J., Westphal, A.J., Huss, G.R., Nagashima, K., Ogliore, R., Brownlee, D.E., Joswiak, D., Tyliszczak, T., and Simionovici, A.S. (2015) Constraints on the formation environment of two chondrule-like igneous particles from comet 81P/Wild 2. Meteoritics and Planetary Science, 50, 976–1004.

Gainsforth, Z., McLeod, A.S., Butterworth, A.L., Dominguez, G., Basov, D., Keilmann, F., Thiemens, M., Tyliszczak, T., and Westphal, A.J. (2013) Caligula, a Stardust sulfide-silicate assemblage viewed through SEM, nanoFTIR, and STXM. 45th Lunar and Planetary Science Conference, 44, 2332.

Gainsforth, Z., Ogliore, R.C., Bustillo, K., Westphal, A.J., and Butterworth, A.L. (2014) Ni zoned nano-pyrrhotite from Stardust Track C2062,2,152 (Cecil). 45th Lunar and Planetary Science Conference, 2637.

Harries, D., and Langenhorst, F. (2013) The nanoscale mineralogy of Fe,Ni sulfides in pristine and metamorphosed CM and CM/CI-like chondrites: Tapping a petrogenetic record. Meteoritics and Planetary Science, 48, 879–903.

Harries, D., Pollok, K., and Langenhorst, F. (2011) Translation interface modulation in NC-pyrrhotites: Direct imaging by TEM and a model toward understanding partially disordered structural states. American Mineralogist, 96, 716–731.

Hunter, J.D. (2007) Matplotlib: A 2D graphics environment. Computing in Science & Engineering, 9, 90–95.

Imae, N. (1994) Direct evidence of sulfidation of metallic grain in chondrites. Proceedings of the Japan Academy. Ser. B: Physical and Biological Sciences, 70, 133–137.

Jacquet, E., Alard, O., and Gounelle, M. (2015) The formation conditions of enstatite chondrites: Insights from trace element geochemistry of olivine-bearing chondrules in Sahara 97096 (EH3). Meteoritics and Planetary Science, 50, 1624–1642.

Larimer, J.W. (1968) An experimental investigation of oldhamite, CaS; and the petrologic significance of oldhamite in meteorites. Geochimica et Cosmochimica Acta, 32, 965–982, https://doi.org/10.1016/0016-7037(68)90061-6.

Lauretta, D.S. (2005) Sulfidation of an iron–nickel–chromium–cobalt–phosphorus alloy in 1% H_2S–H_2 gas mixtures at 400–1000 °C. Oxidation of Metals, 64, 1–22.

Lauretta, D.S., and Buseck, P.R. (2003) Opaque minerals in chondrules and fine-grained chondrule rims in the Bishunpur (LL3.1) chondrite. Meteoritics and Planetary Science, 38, 59–80.

Lauretta, D.S., Kremser, D.T., and Fegley, B.J. (1996) The rate of iron sulfide formation in the solar nebula. Icarus, 122, 288–315.

Lauretta, D.S., Lodders, K., and Fegley, B.J. (1997) Experimental simulations of sulfide formation in the solar nebula. Science, 277, 358–360.

Lehner, S.W., Buseck, P.R., and McDonough, W.F. (2010) Origin of kamacite, schreibersite, and perryite in metal-sulfide nodules of the enstatite chondrite Sahara 97072 (EH3). Meteoritics and Planetary Science, 45, 289–303.

Lewis, J.S. (1972) Low temperature condensation from the solar nebula. Icarus, 16, 241–252.

Li, Y., and Audétat, A. (2012) Partitioning of V, Mn, Co, Ni, Cu, Zn, As, Mo, Ag, Sn, Sb, W, Au, Pb, and Bi between sulfide phases and hydrous basanite melt at upper mantle conditions. Earth and Planetary Science Letters, 355-356, 327–340.
Lodders, K. (2010) Solar system abundances of the elements. Principles and Perspectives in Cosmochemistry, pp. 379–417.
Lord, H.C. III (1965) Molecular equilibria and condensation in a solar nebula and cool stellar atmospheres. Icarus, 4, 279–288.
Mackinnon, I., and Rietmeijer, F. (1987) Mineralogy of chondritic interplanetary dust particles. Reviews of Geophysics, 25, 1527–1553.
MacLean, W.H., and Shimazaki, H. (1976) The partition of Co, Ni, Cu, and Zn between sulfide and silicate liquids. Economic Geology, 71, 1049–1057.
Nakazawa, H. and Morimoto, N. (1971) Phase relations and superstructures of pyrrhotite, $Fe_{1-x}S$. Materials Research Bulletin, 6, 345–357.
Narita, T., and Nishida, K. (1973) On the high-temperature corrosion of Fe-Cr alloys in sulfur vapor. Oxidation of Metals, 6, 157–180.
Ogliore, R.C., Butterworth, A.L., Fakra, S.C., Gainsforth, Z., Marcus, M.A., and Westphal, A.J. (2010) Comparison of the oxidation state of Fe in comet 81P/Wild 2 and chondritic-porous interplanetary dust particles. Earth and Planetary Science Letters, 296, 278–286.
Ogliore, R.C., Butterworth, A.L., and Gainsforth, Z. (2012) Sulfur isotope measurements of a Stardust fragment. 40th Lunar and Planetary Sciences Conference, 1670.
Okada, A., Kobayashi, K., Ito, T., and Sakurai, T. (1991) Structure of synthetic perryite, $(Ni,Fe)_8(Si,P)_3$. Acta Crystallographica, C47, 1358–1361, doi:10.1107/S0108270191000483.
Oliphant, T.E. (2007) Python for scientific computing. Computing in Science & Engineering, 9, 10–20.
Osaka, T., Nakazawa, H., Hatano, T., and Sakaguchi, K. (1976) Formation of iron sulfide fine particles by evaporation in argon gas. Journal of Crystal Growth, 34, 92–102.
Pérez, F., and Granger, B.E. (2007) IPython: A system for interactive scientific computing. Computing in Science & Engineering, 9, 21–29.
Pósfai, M., Sharp, T.G., and Kontny, A. (2000) Pyrrhotite varieties from the 9.1 km deep borehole of the KTB project. American Mineralogist, 85, 1406–1415.
Pratt, A.R., Muir, I.J., and Nesbitt, H.W. (1994) X-ray photoelectron and Auger electron spectroscopic studies of pyrrhotite and mechanism of air oxidation. Geochimica et Cosmochimica Acta, 58, 827–841.
Putnis, A. (1975) Observations on coexisting pyrrhotite phases by transmission electron microscopy. Contributions to Mineralogy and Petrology, 52, 307–313.
Schrader, D.L., McCoy, T.J., and Davidson, J. (2015) Widespread evidence for high-temperature formation of pentlandite in chondrites. Meteoritics and Planetary Science, 46, 1604.
Stodolna, J., Gainsforth, Z., Butterworth, A.L., and Westphal, A.J. (2014) Characterization of preserved primitive fine-grained material from the Jupiter family comet 81P/Wild 2—A new link between comets and CP-IDPs. Earth and Planetary Science Letters, 388, 367–373.
Swartzendruber, L.J., Itkin, V.P., and Alcock, C.B. (1991) The Fe-Ni (iron-nickel) system. Journal of Phase Equilibria, 12, 288–312.
Tamura, N. (2014) XMAS: A versatile tool for analyzing synchrotron X-ray microdiffraction data. In R. Barabash and G. Ice, Eds., Strain and Dislocaton Gradients from Diffraction Spatially-Resolved Local Structure and Defects, p. 125–155. Imperial College Press, London.
Tamura, N., Kunz, M., Chen, K., Celestre, R.S., MacDowell, A.A., and Warwick, T. (2009) A superbend X-ray microdiffraction beamline at the advanced light source. Materials Science and Engineering A, 524, 28–32.
Van Der Walt, S., Colbert, S.C., and Varoquaux, G. (2011) The NumPy array: A structure for efficient numerical computation. Computing in Science & Engineering, 13, 22–30.
Van Dyck, D., Broddin, D., Mahy, J., and Amelinckx, S. (1987) Electron diffraction of translation interface modulated structures. Physica status solidi (a), 103, 357–373.
Wang, H., and Salveson, I. (2005) A review on the mineral chemistry of the non-stoichiometric iron sulphide, $Fe_{1-x}S$ ($0 \le x \le 0.125$): polymorphs, phase relations and transitions, electronic and magnetic structures. Phase Transitions, 78, 547–567.
Westphal, A.J., Fakra, S.C., Gainsforth, Z., Marcus, M.A., Ogliore, R.C., and Butterworth, A.L. (2009) Mixing fraction of inner solar system material in Comet 81P/Wild2. The Astrophysical Journal, 694, 18–28.
Williamson, G., and Hall, W. (1953) X-ray line broadening from filed aluminium and wolfram. Acta Metallurgica, 1, 22–31.
Wojdyr, M. (2010) Fityk: a general-purpose peak fitting program. Journal of Applied Crystallography, 43, 1126–1128.
Yund, R.A., and Hall, H.T. (1969) Hexagonal and monoclinic pyrrhotites. Economic Geology, 64, 420–423.
Zhang, K., Zheng, H., Wang, J., and Wang, R. (2008) Transmission electron microscopy on iron monosulfide varieties from the Suizhou meteorite. Physics and Chemistry of Minerals, 35, 425–432.
Zolensky, M.E., and Thomas, K.L. (1995) Iron and iron-nickel sulfides in chondritic interplanetary dust particles. Geochimica et Cosmochimica Acta, 59, 4707.

Manuscript received May 6, 2016
Manuscript accepted May 23, 2017
Manuscript handled by Rhian Jones